THE ROYAL
SOCIETY

A many-component lattice Boltzmann equation simulation for transport of deformable particles

By M. M. Dupin, T. J. Spencer, I. Halliday and C. M. Care

Materials Research Institute, Sheffield Hallam University, Howard Street, Sheffield S1 1WB, UK (mriih@exchange.shu.ac.uk)

We review the analysis of single and N-component lattice Boltzmann methods for fluid flow simulation. Results are presented for the emergent pressure field of a single phase incompressible liquid flowing over a backward-facing step, at moderate Reynolds Number, which is compared with the experimental data of Denham & Patrick (1974 *Trans. IChE* **52**, 361–367). We then access the potential of the N-component method for transport of high volume fraction suspensions of deformable particles in pressure-driven flow. The latter are modelled as incompressible, closely packed liquid drops. We demonstrate the technique by investigating the particles' transverse migration in a uniform shear ('lift'), and profile blunting and chaining.

Keywords: lattice Boltzmann; *N*-component flow; blunting; pressure-driven flow

1. Introduction

The expanding literature on the lattice Boltzmann method (hereafter LBM) may be classified into general model development (use) in simple (complex) geometry, turbulence, thermohydrodynamics and complex, N-component fluids. Simple geometries are used for quantitative comparisons or qualitative tests of new schemes. Typical of the latter, Hou *et al.* (1995) and Hou (1995) compare LBM and computational fluid dynamics (hereafter CFD) results for lid-driven cavity flow for a range of Reynolds numbers $10 \leqslant Re \leqslant 10^5$. Other geometries include backward-facing steps and arrays of cylinders (Qian *et al.* 1996; He & Luo 1997*a*; Chen *et al.* 1997), for both creeping and vortex shedding. Several informative reviews can be found (see, for example, Wagner 1994; Higuera & Luo 1989; Mei *et al.* 2000). Relative ease of boundary implementation makes LBM well suited for complex geometries. Typical of this application is work by He & Doolen (1997*a*, *b*), who also use an irregular lattice and an interpolation system. In porous media, the LBM's application to the problem of the emergence of macroscopic transport coefficients from microscopic dynamics has demonstrated its mesoscale credentials. Darcy's law has been confirmed in LBM schemes by Succi *et al.* (1989), Cali *et al.* (1992) and Ferreol & Rothman (1995). Fundamental LBM development is now a large area of research encompassing boundary models, numerical stability (Reider & Sterling 1995), non-uniform grids (He & Doolen 1997*a*, *b*; Filippova & Hänel 1998; Tölke *et al.* 1998) and spurious dynamics (Qian & Zhou

Phil. Trans. R. Soc. Lond. A (2004) **362**, 1885–1914

© 2004 The Royal Society

1885

1998). Several turbulence models are currently available (Martinez *et al.* 1994; Succi *et al.* 1991; Hou *et al.* 1996) and these may be coupled with thermohydrodynamic models (see below). Further afield, LBM models for the Schrödinger equation are under development (Succi 2002; Boghosian & Taylor 1997).

LBMs for fluids with an energy mode were initially developed by Alexander *et al.* (1993), to model monotonic gases. Subsequent improvements (Chen *et al.* 1994) have produced a model which agrees well with analytical results for Couette and Poiseuille flows. However, these thermohydrodynamic LBM models only allow small temperature variations, due to their limited stability arising from the lack of an H-theorem.

Simulating complex fluids is a strength of the LBM. Colloids have been considered with algorithmic generalizations to represent suspended particles (Ladd 1994), and other LBM models include magnetohydrodynamics (Chen *et al.* 1991), bubble growth (Yang *et al.* 2001) and granular flows (Luo *et al.* 1997). Most importantly for this work, two-phase fluids with spontaneous interface formation have been developed to model immiscible fluids (Swift *et al.* 1995; Gunstensen *et al.* 1991; Shan & Chen 1994; Halliday *et al.* 1998; Lishchuk *et al.* 2003), and, for N immiscible components ($N \gg 2$) by Dupin *et al.* (2003). It is on this area that we shall now concentrate.

Currently, LBM models fluid mixtures using two strategies, broadly termed 'bottom up' and 'top down'. On one hand, top-down strategies are adopted when appropriate behaviour may be postulated for the model: the system considered (often mesoscale) has an interface with a known equilibrium state. Free-energy LBM interface models (Swift *et al.* 1995) capture the kinematics and hydrodynamics of phase separation, for example. On the other hand, bottom-up strategies are adopted where hydrodynamics alone defines a continuum problem (as in the present work), or where, for very complicated systems, an equilibrium state of the interface is not known. In the latter case simpler LBM interface algorithms are equally valid (Do-Quang *et al.* 2000) and desirable from several points of view: computational efficiency (Dupin *et al.* 2003), their ability to embed additional physics directly and their ability to produce a sharp fluid–fluid interface which impacts minimally on the continuum length-scales of the application. A range of techniques has been developed to model such fluid interfaces with, perhaps, the Shan & Chen (1994) approach being the most popular. More details can be found in reviews by Benzi *et al.* (1992) and Chen & Doolen (1998).

In continuum hydrodynamics, the boundary between immiscible fluids should have no structure. However, surface tension in the (*mesoscale*) LBM is activated by methods which are *microscopic* and as a consequence, the emergent LBM interface has artefacts: small but spurious velocities or micro-currents and a finite thickness. It should be noted that another scheme for imposing surface tension by Lishchuk *et al.* (2003) has a greatly reduced micro-current activity. Here we aim to illustrate the potential of the two-dimensional N-component LBM applied to the transport of high-volume-fraction suspensions of deformable particles in internal pressure-driven flow. We model the latter particles as mutually immiscible, relatively viscous drops of incompressible liquid.

The paper is essentially divided into three further parts. We firstly review the core LBM method (§ 2). Secondly, we present an appropriate generalization, inserting practical immiscibility between a large number of drop species, in § 3. Finally, in § 4, we validate pressure-driven single-component flow with experimental evidence and

proceed to consider N-component problems such as transverse migration on single, deformable drops in a linear shear and the transport of dense suspensions. For the experienced reader, all new results/analysis are to be found there.

2. The Lattice Boltzmann equation for single-component fluids

There are several approaches to the modelling of fluid systems. Microscopic approaches ($<10^{-9}$ m) include molecular dynamics (MD) and non-equilibrium molecular dynamics (NEMD), mesoscale approaches ($<10^{-6}$ m) include lattice gas cellular automaton (LGCA) and lattice Boltzmann and macroscopic approaches ($>10^{-9}$ m) include the broad family of traditional CFD. This section proposes briefly to set the LBM into context and length-scale. For more detail the reader is directed to excellent, comprehensive reviews by Succi (2001), Chen & Doolen (1998) and Luo (2000).

(*a*) *Practical context of the lattice Boltzmann simulation*

At the microscopic scale, MD and NEMD (Goodfellow 1991; Allen & Tildesley 1997) solve numerically the Newtonian equations of motion for a set of explicitly modelled molecules. Both of these techniques show great potential but are impractical for continuum systems: current computer ability limits simulations to only $\sim 10^5$ molecules, *far* short of continuum scales. To bridge the gap, mesoscale methods like dissipative particle dynamics (DPD), Stokesian and Brownian dynamics and LGCA and LBM have evolved.

DPD simulation (Groot & Warren 1997; Español 2002) was originally developed by Hoogerbrugge & Koelman (1992) to avoid the lattice artefacts of LGCA (§ 2 *e*), while accessing hydrodynamic time- and space-scales. In DPD, point-like 'particles' move and interact with each other through prescribed conservative, repulsive, dissipative and stochastic forces whose amplitudes are governed by a fluctuation-dissipation theorem. These particles represent a population of molecules moving coherently. DPD is effectively a coarse graining of MD to a hydrodynamic mesoscale which can accommodate additional microphysics (possibly in the form of potentials) in the interest of multi-phase flows, colloids, and polymers. However, like MD, DPD is computationally expensive. Moreover, problems remain regarding its equation of state, diffusion coefficients and length-scale separations.

The LBM (Chen & Doolen 1998; Succi 2001) uses a discretized Boltzmann equation (§ 2 *g*) with fully discretized space, time and therefore velocity. Distributed groups of particles (hereafter densities) with the same discrete velocity move along links of a lattice and are redistributed at nodes, according to local collision rules. This locality brings decisive advantages to LBM: it is massively parallelizable, complex geometries are made trivial, and additional physics can be included.

In fact the LBM can be used, as in this paper, at continuum scales. However, by far the most popular single-component continuum-scale method remains CFD (Anderson 1995; Conner & Brebbia 1976).

(*b*) *Hydrodynamics of the lattice Boltzmann method*

We shall see that the macroscopic dynamics describing a standard LBM is a weakly compressible form of the Navier–Stokes (Landau & Lifshitz 1995) and continuity

equations

$$\partial_t(\rho) + \partial_\beta(\rho u_\beta) = 0, \tag{2.1}$$

$$\partial_t(\rho u_\alpha) + \partial_\beta(\rho u_\alpha u_\beta) = -\partial_\alpha P + \partial_\beta(2\nu\rho S_{\alpha\beta}) + \rho a_\alpha, \tag{2.2}$$

where a_α is a uniform acceleration acting on the lattice fluid, ν its kinematic viscosity, P the lattice fluid pressure, ρ the lattice fluid's density, $S_{\alpha\beta} = \frac{1}{2}(\partial_\beta u_\alpha + \partial_\alpha u_\beta)$ the rate of strain tensor and $\boldsymbol{u}$ the lattice fluid's velocity (see equation (2.20) for the definition of ρ and $\boldsymbol{u}$). The LBM has an ideal gas equation of state,

$$P = c_s^2 \rho, \tag{2.3}$$

where c_s^2 is the speed of sound squared. Equations (2.1) and 2.2 have solutions parametrized by a single dimensionless number, based on a characteristic lattice velocity U_0, lattice dimension L_0 and the LBM's kinematic viscosity ν: the lattice Reynolds number

$$Re = \frac{U_0 L_0}{\nu}, \tag{2.4}$$

which quantity may be directly compared with the Reynolds number of the flow under study. Note that, for LBM, the speed of sound c_s is only $O(1)$, which induces some problems for high-Re applications of the standard LBM.

(c) Theoretical foundations of the lattice Boltzmann method

The earliest example of LBM (*ca.* 1988) was essentially an attempt to address statistical noise inherent in LGCA (Succi 2001). Subsequently, the essential theoretical basis of the LBM has been shown to derive from non-equilibrium statistical mechanics (Succi 2001, 2002) so its theoretical analysis has two distinct routes. One, heuristic, follows LBM's advent from LGCA's, the other a formal discretization of the exact Boltzmann transport equation (He & Luo 1997b; Abe 1966). We detail the former here.

Boltzmann made stringent assumptions (Liboff *et al.* 2003) to close the description of dilute systems obtained from kinetic theory. For dilute systems the macroscopic observables of interest only depend on one- or two-body distributions, so the $6N$ variables were reduced to just $M = 1, 2$. The Boltzmann equation

$$\partial_t f + \boldsymbol{v} \cdot \partial_{\boldsymbol{x}} f + \boldsymbol{a} \cdot \partial_{\boldsymbol{v}} f = C_2\{f_2\} \tag{2.5}$$

then follows, where $f = f_1(\boldsymbol{x}, \boldsymbol{v}, t)$ is the one-body distribution representing the probability density of finding a particle at position $\boldsymbol{x}$, with particle velocity $\boldsymbol{v}$ at time t. f_2 is a two-body distribution (see below) and C_2 is the two-body-collision operator. It should be noted that, for dense systems, the validity of this reduction is less clear and, at the time of writing, there are attempts to formulate lattice BBGKY equations (after Bogolyubov, Born, Green, Kirkwood and Yvon), which may be better adapted to the simulation of denser fluids. The left-hand side of equation (2.5) represents the free steaming of particles in phase space; the collision operator, $C_2\{f_2\}$, henceforth denoted $C(f, f)$, on the right, represents the effects of collisions. In the dilute-gas limit (where binary collisions alone are significant) the gas is considered to be subjected to molecular chaos (molecules entering a binary collision have uncorrelated motion):

$$f_2(\boldsymbol{x}_1, \boldsymbol{v}_1, \boldsymbol{x}_2, \boldsymbol{v}_2, t) = f(\boldsymbol{x}_1, \boldsymbol{v}_1, t)f(\boldsymbol{x}_2, \boldsymbol{v}_2, t). \tag{2.6}$$

This allowed Boltzmann to write down an integral expression for the $C_2\{f_2\}$ (Liboff *et al.* 2003). In fact He & Luo (1997a) have shown that one particular LBE algorithm may be obtained by a systematic discretization of equation (2.5).

(d) Solving the Boltzmann equation: Chapman–Enskøg analysis

The Chapman–Enskøg procedure is used to solve the Boltzmann equation (2.5) by means of recursive perturbation techniques (Chapman & Cowling 1970). A variant of this method might be better known as 'successive approximation', 'multi-scale expansion' or 'Hilbert expansion'. It is used to obtain the behaviour of hydrodynamic modes in the LBM, although crucially, it may miss other, kinetic, modes. The expansion is parametrized by a small dimensionless Knudsen number, Kn, introduced into the collision term of the Boltzmann equation (2.5) without the forcing term (Liboff *et al.* 2003):

$$\partial_t f + v_\alpha \partial_\alpha f = \frac{1}{\varepsilon} C(f, f), \quad \varepsilon \equiv Kn = \frac{l}{L}. \tag{2.7}$$

The distribution function $f(\boldsymbol{x}, \boldsymbol{v}, t)$ and time derivative are then expanded in terms of ε as

$$f = \sum_{n=0}^{\infty} \varepsilon^n f^{(n)}, \qquad \partial_t = \sum_{n=0}^{\infty} \varepsilon^n \partial_{t_n}, \tag{2.8}$$

with the constraints that 'moments' of the *equilibrium distribution* $f^{(0)}$,

$$f^{(0)} = f^{(\mathrm{eq})} = \frac{\rho}{(2\pi RT)^{D/2}} \exp\left\{ -\frac{(\boldsymbol{v} - \boldsymbol{u})^2}{2RT} \right\}, \tag{2.9}$$

alone determine the hydrodynamic quantities

$$\left. \begin{aligned} \int f^{(0)} \begin{bmatrix} 1 \\ \boldsymbol{v} \\ \frac{1}{2}(\boldsymbol{v} - \boldsymbol{u})^2 \end{bmatrix} \mathrm{d}\boldsymbol{v} = \rho \begin{bmatrix} 1 \\ \boldsymbol{u} \\ e \end{bmatrix} \\ \int \varepsilon^{(n)} f^{(n)} \begin{bmatrix} 1 \\ \boldsymbol{v} \\ \frac{1}{2}(\boldsymbol{v} - \boldsymbol{u})^2 \end{bmatrix} \mathrm{d}\boldsymbol{v} = 0, \quad n > 0, \end{aligned} \right\} \tag{2.10}$$

where e is the energy and $\boldsymbol{u}$ is the macroscopic fluid velocity. Importantly, higher-order non-equilibrium parts ($f^{(n)}$, $n > 0$) do not contribute to the hydrodynamic observable. Note, the space/time variation of $f^{(0)}$ is purely implicit, through, for example, $f^{(0)} = f^{(0)}(\rho, \boldsymbol{u}, T)$. The collision term is also expanded in terms of ε,

$$C(f, f) = \sum_{n=0}^{\infty} \varepsilon^n C^{(n)}, \qquad C^{(n)} = \sum_{k+l=n} C(f^{(k)}, f^{(l)}), \tag{2.11}$$

and solutions to the Boltzmann equation may now be obtained by equating powers of ε in the expanded equation, obtained from equations (2.7)–(2.11), then solving each order of this recursion hierarchically:

$$\left. \begin{aligned} O(\varepsilon^{-1}): & \quad C(f^{(0)}, f^{(0)}) = 0, \\ O(\varepsilon^0): & \quad \partial_t f^{(0)} + v_\alpha \partial_\alpha f^{(0)} = 2C(f^{(0)}, f^{(1)}) \\ & \qquad \qquad \vdots \end{aligned} \right\} \tag{2.12}$$

By solving to $O(\varepsilon^{-1})$, the equilibrium distribution $f^{(0)}$ is found to be the Maxwell–Boltzmann distribution (Chapman & Cowling 1970). Given this, the $O(\varepsilon^0)$ equation can, in principle, yield $f^{(1)}$, and so on through increasing orders of ε.

Hydrodynamic equations are extracted by evaluating moments of the Boltzmann equation with normal solutions (Liboff *et al.* 2003):

$$\int (\partial_t f + v_\alpha \partial_\alpha f - C(f,f)) \, \mathrm{d}\boldsymbol{v} \begin{bmatrix} 1 \\ \boldsymbol{v} \\ \frac{1}{2}(\boldsymbol{v} - \boldsymbol{u}) \end{bmatrix} = 0. \tag{2.13}$$

The above equations will give the Euler equation (Landau & Lifshitz 1995) for $f = f^{(0)}$ and the Navier–Stokes equations (2.2) for $f = f^{(0)} + f^{(1)}$ (Liboff *et al.* 2003).

The Chapman–Enskøg procedure is, unsurprisingly, key to extracting the hydrodynamic equations of the LBM and will be used in detail in § 2 *h*. An important approximation of the Bhatnagar–Gross–Krook (BGK) collision operator (Bhatnagar *et al.* 1954) greatly simplifies solution. The BGK Boltzmann equation is

$$\partial_t f + v_\alpha \partial_\alpha f = -\frac{1}{\tau}(f - f^{(0)}), \tag{2.14}$$

and now the first-order solution $f^{(1)}$ is easily obtained, from equation (2.12), as

$$f^{(1)} = -\tau(\partial_t f^{(0)} + v_\alpha \partial_\alpha f^{(0)}). \tag{2.15}$$

(*e*) *Lattice gas cellular automata*

It is instructive to look at the construction of lattice gas cellular automata (LGCA) models, as these are parents to the LBM and operate in a similar vein.

Cellular automata (CA) (von Neumann 1966) and MD for gases (Broadwell 1964) were merged to gave rise to the first LGCA. Mono-energetic molecules are confined to move/interact on a lattice and updated by CA rules. Space, velocity and time are all discretized. The first LGCA model (the HPP model) with deterministic rules that reproduce fluid dynamic-like features was introduced by Hardy, de Pazzis and Pomeau (Hardy *et al.* 1973, 1976). This was superseded by the FHP model (proposed by Frisch, Hasslacher and Pomeau (Frisch *et al.* 1986; Wolfram 1986)), which was the first LGCA model shown to map onto the Navier–Stokes equations (2.2). It has discrete velocity and position space and discrete collision rules (Frisch *et al.* 1986), represented in essence in figure 1, which shows two sequential lattice states.

Notwithstanding, evolution of the LGCA models is very simple and consists of two main repeated steps: collision and streaming (see figure 1), the time-order of which is irrelevant. Collisions are very simple but must conserve particle number, momenta and energy (only). Evolution is represented by a lattice-species Boltzmann equation

$$n_i(\boldsymbol{x} + \boldsymbol{c}_i, t + 1) - n_i(\boldsymbol{x}, t) = C_i(n_1, n_2, \ldots), \tag{2.16}$$

where $n_i(\boldsymbol{x}, t)$ is the number $\in \{0, 1\}$ of particles with particle velocity $\boldsymbol{c}_i, n_i \in \{0, 1\}$; the subscripts i and j denote discrete velocities $i, j \in \{1, 2, \ldots, b\}$, b is the size of the lattice velocity basis and $\boldsymbol{c}_i$ is a 'Boolean' function of the n_i values which expresses the possible collisions.
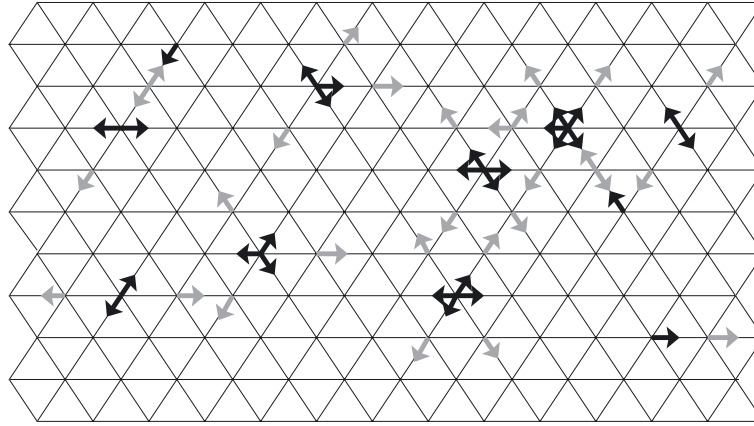
Figure 1. Lattice structure and evolution of the FHP-I LGA model. Solid (hollow) arrows represent particles with the velocities corresponding to time t ($t+$). Hollow arrows therefore represent post collision, post propagation evolution.

The LGCA may be viewed as a maximally discretized MD model. Variants with increased stability on more complicated lattices have been developed: essentially, all give the same general hydrodynamic equations but with different values for, e.g., the speed of sound squared c_s^2 and lattice fluid viscosities ν and η. The key advantages of LGCAs are their unconditional stability, optimal use of computer memory, and localization, allowing for massive parallelization and dedicated computers. In fact it has been shown that isothermal LGCA models admit both a local and global H-theorem (Frisch *et al.* 1986), confirming the unconditional stability—a decisive advantage in the computation of turbulence. Further information on LGCA and its applications may be found in Succi (2001), Wolfram (1986), He *et al.* (1997*a*), McNamara & Zanetti (1988), D'Humières *et al.* (1989), Rothmann & Zaleski (1994) and Benzi *et al.* (1992).

LGCA simulation has now been largely superseded by the LBM, for the above advantages are accompanied by a number of limitations. Certainly, early models were limited to relatively low Reynolds numbers (see equation (2.4)) due to high momentum diffusivity (viscosity ν) and the LGCA's lack of Galilean invariance.

(*f*) *Lattice Boltzmann models*

McNamara & Zanetti (1988) realized that equation (2.16) can be re-expressed as a Boltzmann equation for LGCA ensemble averages. Defining

$$f_i(\boldsymbol{x}, t) \equiv \langle n_i(\boldsymbol{x}, t) \rangle, \quad 0 \leqslant f_i \leqslant 1, \; i = 1, \dots, b, \tag{2.17}$$

where $f_i(\boldsymbol{x}, t)$ are real continuous functions representing the probability distribution of finding particles with discrete velocities and space. Their evolution may be expressed after equation (2.16) as

$$f_i(\boldsymbol{x} + \boldsymbol{c}_i, t + 1) - f_i(\boldsymbol{x}, t) = \Delta_i(f_0, f_1, f_2, \dots), \tag{2.18}$$

the collision term $\Delta_i(f_i)$ being essentially the C_i of the LGCA but with the ensemble averages f_i replacing the n_i (Frisch *et al.* 1986). In fact, there are several variants of the lattice Boltzmann method (e.g. Succi 2002); we shall focus on the simplest.
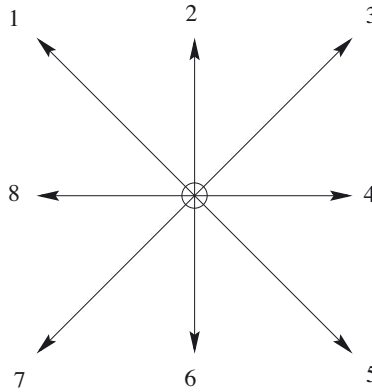
Figure 2. The D2Q9 model lattice structure showing a regular repeating structure
with nine distributions located at each lattice node.

(g) Lattice BGK (LBGK) models

It was Qian *et al*. (1992) and Chen *et al*. (1992) who realized that Δ_i in (2.17) could be further simplified by assuming a singe relaxation time τ:

$$f_i(\boldsymbol{x} + \delta\boldsymbol{c}_i, t + \delta) = f_i(\boldsymbol{x}, t) - \frac{1}{\tau}(f_i(\boldsymbol{x}, t) - f_i^{(\mathrm{eq})}) + F_i, \quad 0 \leqslant \frac{1}{\tau} \leqslant 2, \qquad (2.19)$$

in which we have added a 'forcing term', F_i, to which we shall return, taking $F_i = 0$ for the moment. Note that equation (2.19) has a relaxation form.

Equation (2.19) and its appropriate equilibrium distribution function (see below) together comprise the so-called LBGK model. Setting $\tau = 1$ in equation (2.19), the momentum densities, f_i, relax immediately to local equilibrium $f_i^{(\mathrm{eq})}$, on the scale of the propagation length $\delta c_{i\alpha}$, which is determined by the time-of-flight parameter δ. With $c_{i\alpha} = O(1)$ it is natural to associate the duration δ with the mean free path, or Knudsen number. In other words, we take $\delta = \varepsilon$ (see equation (2.7)) for the purposes of extracting the model's dynamics.

When LBM is used for two-dimensional fluid dynamics simulations, the LBGK model is the one most commonly used and, in particular, the one with nine velocities in two dimensions (D2Q9). Section 2 *h* details an analysis for extracting its hydrodynamics. The shortcomings of the LBGK models include spurious invariant quantities when $1/\tau$ reaches its limits, and round-off errors which can cause instability, due to floating point algebra. At present no local or global H-theorem for LBM models has been found (Succi 2002). However, it is anticipated that this will change in the near future. This will allow the stability boundaries for these methods to be determined.

(h) Hydrodynamics of the LBGK method

Our method of manipulating the macroscopic dynamics differs from that of others (e.g. Hou *et al*. 1995) in that, for adaptability, it treats the role of the lattice in a general way. However, we focus on the slow, hydrodynamic modes in the usual way, by using a Chapman–Enskøg analysis to develop the LBGK evolution equation, (2.19). The requirements on $f_i^{(n>0)}$ are as discussed previously, but we have an additional

requirement that the second moment of $f_i^{(1)}$ relates directly to the viscous stress $\Pi_{\alpha\beta}^{(1)}(x_\alpha, t)$:

$$\left.\begin{aligned}\sum_i f_i^{(\text{eq})} \begin{bmatrix} 1 \\ c_{i\alpha} \\ c_{i\alpha}c_{i\beta} \end{bmatrix} &= \begin{bmatrix} \rho(\boldsymbol{x}, t) \\ \rho u_\alpha(\boldsymbol{x}, t) \\ \Pi_{\alpha\beta}^{(0)}(\boldsymbol{x}, t) \end{bmatrix}, \\[2mm] \sum_i f_i^{(n)} \begin{bmatrix} 1 \\ c_{i\alpha} \\ c_{i\alpha}c_{i\beta} \end{bmatrix} &= \begin{bmatrix} 0 \\ 0 \\ \Pi_{\alpha\beta}^{(n)}(\boldsymbol{x}, t) \end{bmatrix}, \quad n > 0.\end{aligned}\right\} \tag{2.20}$$

In fact LBGK equilibrium $f_i^{(\text{eq})}$ approximates a uniformly translating Maxwell–Boltzmann distribution in the peculiar velocity $(c_{i\alpha} - u_\alpha)$:

$$\left.\begin{aligned}f_i^{(\text{eq})} &= \frac{\rho}{(2\pi RT)^{D/2}} \exp\left\{-\frac{(c_{i\alpha} - u_\alpha)^2}{2RT}\right\} = \rho t_i \exp\left\{\frac{u_\alpha c_{i\alpha}}{RT}\right\} \exp\left\{-\frac{u^2}{2RT}\right\}, \\[2mm] t_i &\equiv \exp\left\{\frac{c_{i\alpha}c_{i\alpha}}{RT}\right\} \frac{1}{(2\pi RT)^{D/2}},\end{aligned}\right\} \tag{2.21}$$

by making a Taylor expansion to $O(u^2)$ in equation (2.21):

$$f_i^{(\text{eq})} = \rho t_i \left(1 + \frac{c_{i\alpha}u_\alpha}{RT} + \frac{c_{i\alpha}c_{i\beta}u_\alpha u_\beta}{2(RT)^2} - \frac{u^2}{2RT}\right).$$

For isothermal flows R and T are constant and we therefore may simplify $f_i^{(\text{eq})}$:

$$f_i^{(\text{eq})} = t_i(A + Bc_{i\alpha}u_\alpha + Cc_{i\alpha}c_{i\beta}u_\alpha u_\beta + Du^2), \tag{2.22}$$

in which t_i, A, B, C and D are taken as constants yet to be determined (not all of which are independent). This form of the equilibrium distribution is less general than that of Hou *et al.* (1995), because it is predicated, from the outset, on a uniformly translating Maxwell–Boltzmann. However, any attempt to depart significantly from that form (i.e. that of equation (2.22)) quickly leads to instabilities. In the limit of small Re, an increased freedom of choice around the coefficients in equation (2.22) is a means of embedding different physical effects. Our discrete velocity set $\boldsymbol{c}_i$ is that of the most popular in the literature, classified D2Q9 (two dimensions and nine discrete velocities; see figure 2). Here we derive parameters for D2Q9, though it is trivial to adapt this derivation to fit any of the models listed at the end of this section.

To close the equilibrium distribution $f_i^{(\text{eq})}$ of our D2Q9 model (and effectively determine the whole of the model's dynamics) we Taylor expand the left-hand side of the LBGK evolution equation (2.19) to second order in $\delta = \varepsilon$ as

$$\varepsilon[\partial_t + c_{i\alpha}\partial_\alpha]f_i + \tfrac{1}{2}\varepsilon^2[\partial_t + c_{i\alpha}\partial_\alpha]^2 f_i + O(\varepsilon^3) = -\frac{1}{\tau}(f_i - f_i^{(\text{eq})}). \tag{2.23}$$

The terms of $O(\varepsilon)$ already correspond to the Boltzmann transport equation (2.14). We now substitute the Knudsen number ε-expansions of equations (2.8) (for f_i about equilibrium $f_i^{(\text{eq})}$ and for the time derivative ∂_t about ∂_{t_0}) into equation (2.23) and retain terms to $O(\varepsilon^2)$. Separating orders of ε, we have, at $O(\varepsilon)$,

$$(\partial_{t_0} + c_{i\alpha}\partial_\alpha)f_i^{(0)} = -\frac{1}{\tau}f_i^{(1)}, \tag{2.24}$$

and, at $O(\varepsilon^2)$, using the result at $O(\varepsilon)$ in equation (2.24),

$$\partial_{t_1} f_i^{(0)} + (\partial_{t_0} + c_{i\alpha}\partial_\alpha)\left(1 - \frac{1}{2\tau}\right)f_i^{(1)} = -\frac{1}{\tau}f_i^{(2)}. \tag{2.25}$$

We proceed to tune the discrete moments of equations (2.24) and (2.25) onto hydrodynamic behaviour. Summing equation (2.20) on link index i:

$$\partial_{t_0}\sum_i f_i^{(0)} + \partial_\alpha\sum_i c_{i\alpha}f_i^{(0)} = -\frac{1}{\tau}\sum_i f_i^{(1)},$$

from which it is evident that the model's macroscopic dynamics are described by the continuity equation on its shortest time scales t_0:

$$\partial_{t_0}\rho + \partial_\alpha\rho u_\alpha = 0. \tag{2.26}$$

The first moment of equation (2.24) is obtained by multiplying it by $c_{i\alpha}$ prior to summing on i:

$$\partial_{t_0}\sum_i c_{i\alpha}f_i^{(0)} + \partial_\beta\sum_i c_{i\alpha}c_{i\beta}f_i^{(0)} = -\frac{1}{\tau}\sum_i c_{i\alpha}f_i^{(1)}.$$

Hence, we obtain an Euler equation for the momentum,

$$\partial_{t_0}\rho u_\alpha + \partial_\beta \Pi_{\alpha\beta}^{(0)} = 0, \tag{2.27}$$

where $\Pi_{\alpha\beta}^{(0)}$ is that defined in equation (2.20). To extract the longer-time dissipative modes it is necessary to proceed to longer times. Take moments in the $O(\varepsilon^2)$ equation (2.25) and use the identities given by equation (2.20). The zeroth moment immediately yields

$$\partial_{t_1}\rho = 0, \tag{2.28}$$

and, using equations (2.20), its first moment (with $c_{i\alpha}$) yields

$$\left(1 - \frac{1}{2\tau}\right)\partial_\beta \Pi_{\alpha\beta}^{(1)} + \partial_{t_1}\rho u_\alpha = 0. \tag{2.29}$$

The Chapman–Enskøg expansions need to be recombined, in the case of equations (2.27), (2.29) to give the Navier–Stokes equation. To obtain the desired result from this the process we clearly need to control the form $\Pi_{\alpha\beta}^{(0)}$ and $\Pi_{\alpha\beta}^{(1)}$. This is best achieved by expressing the latter directly in terms of the parameters t_i, A, B, C and D of $f_i^{(eq)}$, resulting in expressions which contain 'tensors' such as $\sum_i t_i c_{i\alpha}c_{i\beta}$, for it is possible to show that $\Pi_{\alpha\beta}^{(0)}$ and $\Pi_{\alpha\beta}^{(1)}$ take appropriate form when such tensors are isotropic.

After Wolfram (1986) and C. M. Care (2003, personal communication), we seek

(i) a set of isotropic tensors E^n with order $O(n)$ of the discrete velocity basis ($c_{i\alpha}$, figure 2),

(ii) the appropriate weight of link i, t_i.

The latter tensors appear in the expressions for $\Pi_{\alpha\beta}^{(0)}$ and $\Pi_{\alpha\beta}^{(1)}$. We define and evaluate the following tensors:

$$
\left.
\begin{aligned}
E^{(0)} &\equiv \sum_i t_i = t_0 + 4t_1 + 4t_2, \\
E_\alpha^{(1)} &\equiv \sum_i t_i c_{i\alpha} = 0, \\
E_{\alpha\beta}^{(2)} &\equiv \sum_i t_i c_{i\alpha} c_{i\beta} = (2t_1 + 4t_2)\delta_{\alpha\beta}, \\
E_{\alpha\beta\gamma}^{(3)} &\equiv \sum_i t_i c_{i\alpha} c_{i\beta} c_{i\gamma} = 0, \\
E_{\alpha\beta\gamma\delta}^{(4)} &\equiv \sum_i t_i c_{i\alpha} c_{i\beta} c_{i\gamma} c_{i\theta} = (2t_1 - 8t_2)\delta_{\alpha\beta\gamma\theta} + 4t_2(\delta_{\alpha\beta}\delta_{\gamma\theta} + \delta_{\alpha\gamma}\delta_{\beta\theta} + \delta_{\alpha\theta}\delta_{\beta\gamma}),
\end{aligned}
\right\}
$$
$$
(2.30)
$$

as may be checked by direct computation, using the D2Q9 basis. Note that odd-order tensors $E^{(2n+1)}$ are zero. Only fourth-order tensors are necessary for hydrodynamics. Wolfram shows that the $E_{\alpha\ldots}^n$ will be isotropic if

$$
E_{\alpha\ldots}^{2n+1} = 0, \qquad E_{\alpha\ldots}^{2n} = T^{2n}\Delta_{\alpha\ldots}^{2n}, \tag{2.31}
$$

where tensor $\Delta_{\alpha\ldots}^{2n}$ is defined as (Wolfram 1986)

$$
\Delta^0 = 1, \qquad \Delta_{\alpha\beta}^2 = \delta_{\alpha\beta}, \qquad \Delta_{\alpha\beta\gamma\theta}^4 = \delta_{\alpha\beta}\delta_{\gamma\theta} + \delta_{\alpha\gamma}\delta_{\beta\theta} + \delta_{\alpha\theta}\delta_{\beta\gamma}. \tag{2.32}
$$

Comparing equations (2.32) and definitions (2.30), we obtain

$$
T^0 = t_0 + 4t_1 + 4t_2, \qquad T^2 = 2t_1 + 4t_2, \qquad T^4 = 4t_2, \qquad t_2 = \tfrac{1}{4}t_1. \tag{2.33}
$$

With equations (2.33), we return to the task of manipulating the emerging macroscopic equations into an appropriate form. We evaluate the requisite moments of the equilibrium distribution (equation (2.20)) by inserting the form of $f_i^{(\mathrm{eq})}$ (2.22) and using equations (2.33). For example, the moment $\sum_i f_i^{(0)} = \rho$ gives

$$
-\rho + A\sum_i t_i + Bu_\alpha \sum_i t_i c_{i\alpha} + Cu_\alpha u_\beta \sum_i t_i c_{i\alpha} c_{i\beta} + Du_\alpha u_\alpha \sum_i t_i = 0, \tag{2.34}
$$

which, on substituting for the tensors from equation (2.22), yields

$$
-\rho + AT^0 + Cu^2 T^2 + Du^2 T^0 = 0 \tag{2.35}
$$

after a little algebra. Similarly, the first moment

$$
\sum_i f_i^{(0)} c_{i\gamma} = \rho u_\gamma
$$

and the 'momentum flux' moment

$$
\sum_i f_i^{(0)} c_{i\gamma} c_{i\theta} = P\delta_{\gamma\theta} + \rho u_\gamma u_\theta,
$$

give, respectively,

$$
\left.
\begin{aligned}
-\rho u_\gamma + Bu_\gamma T^2 &= 0, \\
-P\delta_{\gamma\theta} - \rho u_\gamma u_\theta + AT^2\delta_{\gamma\theta} + T^4 Cu^2\delta_{\gamma\theta} + 2T^4 Cu_\gamma u_\theta + Du^2 T^2\delta_{\gamma\theta} &= 0.
\end{aligned}
\right\} \tag{2.36}
$$

Noting that the equations (2.34)–(2.36) must be true for all ρ, u_α, we obtain the following six equations:

$$-\rho + AT^0 = 0, \qquad CT^2 + DT^0 = 0, \qquad -\rho + BT^2 = 0, \left.\begin{array}{c}\\\end{array}\right\}$$
$$-P + AT^2 = 0, \qquad 2CT^4 - \rho = 0, \qquad CT^4 + DT^2 = 0, \qquad (2.37)$$

and, recalling that $A = \rho$, we have a closed system of simultaneous equations with a non-trivial solution:

$$\left.\begin{array}{lll} A = \rho, & T^0 = 1, & t_0 = \frac{4}{9}, \\ B = 3\rho, & T^2 = \frac{1}{3}, & t_1 = \frac{1}{9}, \\ C = \frac{9}{2}\rho, & T^4 = \frac{1}{9}, & t_2 = \frac{1}{36}, \\ D = -\frac{3}{2}\rho, & P = \frac{1}{3}\rho. & \end{array}\right\} \qquad (2.38)$$

We may identify the $\frac{1}{3}$ in the equation of state as the speed of sound squared (c_s^2), in terms of which the equilibrium is often written

$$f_i^{(\mathrm{eq})} = \rho t_i\left(1 + \frac{c_{i\alpha}u_\alpha}{c_s^2} + \frac{c_{i\alpha}c_{i\beta}u_\alpha u_\beta}{2c_s^4} - \frac{u^2}{2c_s^2}\right). \qquad (2.39)$$

Finally, we demonstrate an appropriate form for 'viscous stress' moment $\Pi_{\alpha\beta}^{(1)}$. We need an expression for $f_i^{(1)}$, obtained by rearranging equation (2.24) as

$$\left.\begin{array}{l} \Pi_{\gamma\theta}^{(1)} = \displaystyle\sum_i c_{i\gamma}c_{i\theta}f_i^{(1)} \\[2mm] = -\tau\displaystyle\sum_i c_{i\gamma}c_{i\theta}(\partial_{t_0} + c_{i\lambda}\partial_\lambda)f_i^{(\mathrm{eq})} \\[2mm] = -\tau[-c_s^2 u_\gamma\partial_\theta\rho - c_s^2 u_\theta\partial_\gamma\rho - \partial_\lambda\rho u_\gamma u_\theta u_\lambda + \partial_\lambda\rho u_\gamma c_s^2\delta_{\lambda\theta} + \partial_\lambda\rho u_\theta c_s^2\delta_{\gamma\lambda}], \end{array}\right\}$$
$$(2.40)$$

where identity $[\partial_{t_0}\rho u_\gamma u_\theta = -c_s^2 u_\gamma\partial_\theta\rho - c_s^2 u_\theta\partial_\gamma\rho - \partial_\lambda\rho u_\gamma u_\theta u_\lambda]$ and the continuity equation have been used.

We recombine the four Chapman–Enskøg moment expansions. First the $O(\varepsilon^1)$ and $O(\varepsilon^2)$ continuity equations (2.26), (2.28):

$$(\varepsilon\partial_{t_0} + \varepsilon^2\partial_{t_1})\rho + \varepsilon\partial_\alpha\rho u_\alpha = 0 \quad\Rightarrow\quad \partial_t\rho + \partial_\alpha\rho u_\alpha = 0. \qquad (2.41)$$

Combining the '$c_{i\alpha}$ moment' $O(\varepsilon^1)$ and $O(\varepsilon^2)$ (equations (2.27) and (2.29)) gives

$$\partial_t\rho u_\alpha + \partial_\beta\rho u_\alpha u_\beta = -\partial_\alpha c_s^2\rho + \varepsilon\tfrac{1}{2}c_s^2(2\tau - 1)\partial_\beta 2\rho S_{\alpha\beta} - (\tau - \tfrac{1}{2})\partial_\beta\partial_\gamma\rho u_\alpha u_\beta u_\gamma,$$

where $S_{\alpha\beta} = \frac{1}{2}(\partial_\alpha u_\beta + \partial_\beta u_\alpha)$ is the rate of strain. Defining the viscosity as

$$\nu \equiv \tfrac{1}{2}\varepsilon c_s^2(2\tau - 1), \qquad (2.42)$$

we note an ideal-gas equation of state, with c_s^2 only of the order of 1. Retaining terms to $O(u^2)$,

$$\partial_t\rho u_\alpha + \partial_\beta\rho u_\alpha u_\beta = -\partial_\alpha P + \partial_\beta(2\nu\rho S_{\alpha\beta}). \qquad (2.43)$$

Equations (2.41) and (2.43) are a weakly compressible form of the Navier–Stokes and continuity equations. The procedure by which they have been derived may be applied

Table 1. *LBGK lattice parameters for a selection of commonly used models indicating the lattice shape, velocity directions and equilibrium distribution weights*

model	unit cell	t_0 0	t_1 1	t_2 $\sqrt{2}$	t_3 $\sqrt{3}$	t_4 2	c_s^2	order of isotropy
D1Q3	line	$\frac{2}{3}$	$\frac{1}{6}$	0	0	0	$\frac{1}{3}$	4
D1Q5	line	$\frac{1}{2}$	$\frac{1}{6}$	0	0	$\frac{1}{12}$	1	6
D2Q7	hexagonal	$\frac{1}{2}$	$\frac{1}{12}$	0	0	0	$\frac{1}{4}$	4
D2Q9	square	$\frac{4}{9}$	$\frac{1}{9}$	$\frac{1}{36}$	0	0	$\frac{1}{3}$	4
D2Q13	hexagonal	$\frac{11}{25}$	$\frac{9}{100}$	0	$\frac{1}{300}$	0	$\frac{3}{10}$	6
D3Q15	cubic	$\frac{2}{9}$	$\frac{1}{9}$	0	$\frac{1}{72}$	0	$\frac{1}{3}$	4
D3Q19	cubic	$\frac{1}{3}$	$\frac{1}{18}$	$\frac{1}{36}$	0	0	$\frac{1}{3}$	4
D3Q27	cubic	$\frac{8}{27}$	$\frac{2}{27}$	$\frac{1}{54}$	$\frac{1}{216}$	0	$\frac{1}{3}$	4
D4Q25	FCHC	$\frac{1}{3}$	0	$\frac{1}{36}$	0	0	0	4

to the other lattices summarized in terms of their velocity basis and corresponding weights (table 1). It differs from other derivations (Hou *et al.* 1996) simply in that the isotropy of lattice basis tensors is programmed-in explicitly, which is a procedural advantage when inserting additional microphysics. In considering table 1, it should be noted that the analysis of three speed models produces a sufficient number of constraints to solve the coefficients of the equilibrium distribution. However, our method is not the only path to the LBGK equilibrium. He & Luo (1997*b*) give an *a priori* derivation applicable to any lattice structure. Luo integrates the Boltzmann transport equation, via the method of characteristics, to derive the LBGK evolution equation. A Taylor expanded Maxwell–Boltzmann equilibrium distribution has its weights (t_i) and lattice calculated by a numerical integration, the number of velocities reflecting the order and choice of the polynomial used in the quadrature. Following this route leads to a number of enhanced models with flexible lattice structures (Luo 1998; Mei *et al.* 2000; He *et al.* 1997*a*), and it allows one to add physics directly from kinetic theory and the Boltzmann equation.

(*i*) Boundaries in lattice models

The Navier–Stokes equation is an elliptic equation: it requires the boundary velocity field to be closed to have any solution. This velocity information can be set in equivalent terms, especially at open boundaries, using, for example, pressure and flux conditions. One problem with LBM lattice closure is that the velocity distribution gives D conditions which are not necessarily sufficient to determine appropriate values for all the f_i at a boundary.

Consider first the no-slip zero velocity boundary condition. The velocity of the fluid matches that assumed for the boundary, often zero. Wolfram (1986) showed the simplest operation to reproduce a zero in velocity is the bounce-back condition. f_i which stream onto a wall site have their velocities inverted for the next streaming step. This robust process clearly inserts friction into the fluid and conserves mass but it is only first-order accurate (Kadanoff *et al.* 1989).
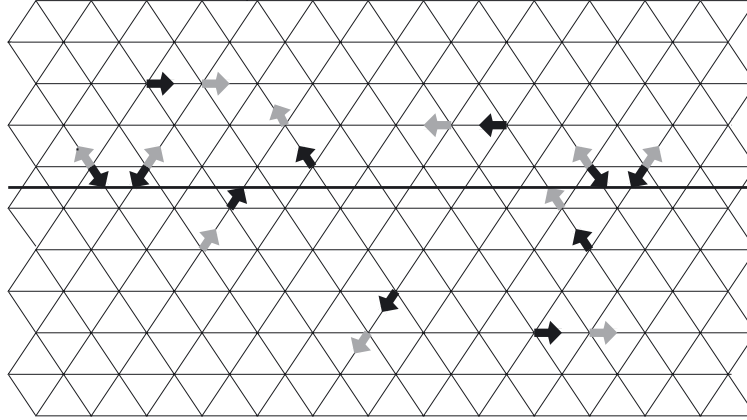
Figure 3. Simplified mid-link bounce-back method on a hexagonal lattice. The heavier line represents the wall position, note it is positioned exactly halfway between lattice nodes. Solid (hollow) arrows represent particle distribution functions at time t $(t+1)$. In one time-step the distribution function effectively travels half a link then bounces back in the reverse direction so as to introduce non-slip boundaries. Both mass and momentum are conserved. To interact with the wall, particles moving in direction i, at the end of time step t, propagate, to re-appear at the same position, moving in direction $i \oplus Q$ (addition modulo Q) at time $t+1$.

The mid-link bounce-back boundary condition retains simplicity of implementation, providing a balance between robustness and accuracy (see figure 3). The zero velocity is located a distance of exactly half a link from the lattice node on which it obtains. It is shown (He *et al.* 1997b; Maier *et al.* 1996; Skordos 1993) to be second-order accurate in space but first-order accurate in time, i.e. not necessarily instantaneously accurate. Note that bounce-back methods are not applicable to open boundaries or moving boundaries.

Halliday *et al.* (2002) proposed strategies for instantaneously accurate lattice closure, for plane boundaries with any known distribution of velocity. Several other sophisticated methods have been developed to overcome the closure problem, all involving velocity gradients (Skordos 1993; Noble *et al.* 1995). All the results presented here use mid-link bounce-back.

For internal pressure-driven flow, pressure and flux conditions often apply at open boundaries. LBM's inherent compressibility error (recall the $O(1)$ speed of sound) allows one to impose internal pressure gradients as gradients in density. This strategy is valid even at modest Re (i.e. when the pressure gradient is large). In isothermal LBM, a simple method of combating compressibility and imposing pressure boundary conditions is to approximate the pressure field to a uniform gradient, which is then represented as a body force (Halliday *et al.* 2001).

More precisely, a uniform body force or acceleration ρa_α may be used to approximate the principal part of a pressure gradient. Such an acceleration can arise in the LBM's momentum equation (§ 2 b) from the term F_i in the lattice evolution equation (2.19). For a uniform body force in an isothermal LBGK (Halliday *et al.* 2001),

$$\sum_i F_i = 0, \qquad \sum_i F_i c_{i\alpha} = \rho a_\alpha, \tag{2.44}$$

and we have, for body force density (acceleration) a_α,

$$F_i = \frac{\rho t_i c_{i\alpha} a_\alpha}{c_s^2}. \tag{2.45}$$

While the above is consistent with Luo's (1998) general derivation of uniform accelerations from the Boltzmann equation, we note that equation (2.45) is strictly valid only if a_α is constant throughout the flow domain. In any system without unidirectional flow, the pressure gradient cannot be uniform. In fact, it must solve a Poisson-type equation obtained by taking the divergence of the incompressible Navier–Stokes equations

$$\nabla^2 \left(\frac{P}{\rho} \right) = \partial_\alpha v_\beta \partial_\beta v_\alpha. \tag{2.46}$$

The solution of (2.46) yields the instantaneous pressure for the given velocity distribution (Succi 2001). Spencer *et al.* (2004) designed a 'two-part' fictitious body force. The first, conservative, part is designed to correct the pressure field after equation (2.46) (see § 4). The second, non-conservative, part is designed, after the method of Halliday *et al.* (2001), to reduce compressibility effects. For applications like those we shall consider, this conservative component closely corresponds to a uniform body force, as the results we present in § 4 will show.

(*j*) *The exactly incompressible LBGK (EILBGK) model in D2Q9*

For slowly varying flows, the problem of compressibility error may be overcome. The EILBGK model of Zou *et al.* (1995) and Lin *et al.* (1996) makes a slight change to the interpretation of the distribution function f_i in order to make the macroscopic dynamics much more incompressible, but at the expense of the accuracy of its time variation. Applications of the EILBGK are therefore restricted to steady-state solutions and to flows with slow variation (low Strouhal number). However, EILBGK allows for a more accurate treatment of pressure boundary conditions. What changes is the equilibrium distribution function and the definition of velocity (other hydrodynamic moments remain unchanged):

$$\left. \begin{aligned} f_i^{(eq)} &= t_i \left(\rho + \frac{c_{i\alpha} u_\alpha}{c_s^2} + \frac{c_{i\alpha} c_{i\beta} u_\alpha u_\beta}{2c_s^4} - \frac{u^2}{2c_s^2} \right), \\ c_s^2 &= \tfrac{1}{3}, \qquad t_0 = \tfrac{4}{9}, \qquad t_1 = \tfrac{1}{9}, \qquad t_2 = \tfrac{1}{36}, \end{aligned} \right\} \tag{2.47}$$

$$\sum_i f_i^{(eq)} \begin{bmatrix} 1 \\ c_{i\alpha} \\ c_{i\alpha} c_{i\beta} \end{bmatrix} = \begin{bmatrix} \rho(x_\alpha, t) \\ u_\alpha(x_\alpha, t) \\ \Pi_{\alpha\beta}^{(0)}(x_\alpha, t) \end{bmatrix}. \tag{2.48}$$

Using the Chapman–Enskøg analysis as in § 2 *h*, one can obtain the following dynamics:

$$\left. \begin{aligned} \partial_\alpha u_\alpha &= 0, \\ \partial_\beta u_\alpha u_\beta &= -\partial_\alpha c_s^2 \rho + \nu \partial_\beta \partial_\beta u_\alpha, \end{aligned} \right\} \tag{2.49}$$

which are the exact steady-state incompressible Navier–Stokes equations with constant density ρ_0. In this model the pressure and viscosity are given by

$$\frac{P}{\rho_0} = c_s^2 \rho, \qquad \nu = \frac{c_s^2}{2}(2\tau - 1), \tag{2.50}$$

in which ρ/ρ_0 is the effective pressure. Note that both the continuity equation and the advective term in the Navier–Stokes equations are exactly incompressible, while the form of the diffusive term is preserved at the cost of the time derivative. In general, EILBGK schemes are not able to achieve the Reynolds numbers of LBGK simulations, due to the stricter incompressibility constraints.

3. Lattice Boltzmann equation for $N \geqslant 2$ immiscible fluids

Here we consider how to insert an appropriate interface between immiscible lattice fluids which are otherwise represented by the D2Q9 model already described. We describe our generalization, to $N \gg 2$ fluids, of an existing model for binary fluids essentially after Gunstensen *et al.* (1991). Our model provides the means to deal, in the hydrodynamic regime, with a very large number of physically different, non-coalescing fluids.

For definiteness, we shall consider the velocity profile of system of stabilized, suspended drops in pressure-driven internal flow (although, of course, our algorithm can be applied more widely). Accordingly, individual drop masses need each to be conserved. In 9.0×10^5 lattice updates of our interface algorithm, the mass of a drop is conserved to better than $2.0 \times 10^{-3}\%$. For simplicity we choose to prevent all suspended/advected drops from wetting the solid boundaries.

Our generalization to N immiscible components assigns each fluid a 'colour' superscript, $\Gamma = 0, 1, 2, 3 \ldots, (N-1)$. Fluids with different values of Γ can have collision parameters τ_Γ and, therefore, different viscosity ν_Γ. Now, for N different species, the N-component LBM quickly demands impractical amounts of computer storage, as N increases. But for relatively small, non-evaporating 'sharp' drops, the storage (arrays) for N primary quantities $f_i^\Gamma(\mathbf{r}, t)$ will be very sparse. Moreover, a natural question arises around the value of attempting to represent, on lattice nodes with Q links (velocities), more than Q different colours or species.

To address storage, we record only $N_Q < Q \ll N$ dominant species at any node. Essentially, we deal with colour difference, as opposed to absolute colour—which generates considerable reduction in the requisite storage. The sharp interfaces from our Gunstensen–type interface method mean minimal mixing and a reduction in the number of different colours found on a node. In practice we take $N_Q = 5$. This value is found to be adequate for even the most intimate mono-disperse N-component flows. Note, however, that this choice reflects the geometry and number of components (colours/drops) in our particular application. Also note that the particular N_Q dominating colours, or immiscible components, vary between nodes and in time. We assign each colour distribution a superscript α, identifying their fluid belonging within the fluids (Γ) of the node.

To guide species segregation, a lattice map of absolute colour, label l, is needed. However, for such a map, sufficient information can be stored in a five-dimensional integer array with subscript set $\{x, y, i, \alpha\}$ to identify, for lattice position $\{x, y\}$ direction i, the n $(< N_Q)$ colours present by the value of integer superscript, α. We have the following limits for the f and the associated colour label l values:

$$0 < f(x, y, i, \alpha), \qquad 0 < l(x, y, i, \alpha) < N,$$

where, for a system of size $L \times W$,

$$0 < x < L, \qquad 0 < y < W, \qquad 0 < i < Q, \qquad 0 < \alpha < N_Q.$$

By recording only a maximum of N_Q species at each node, for a total of N drops (or immiscible components), the dominant (type real) storage requirements ($f_i^\alpha(\boldsymbol{r}, t)$) are reduced by a factor N_Q/N, to levels comparable with the diphasic model (Gunstensen *et al.* 1991).

In our N-phase model, collision is, as in the diphasic model, performed in three steps: mixed fluid collision, perturbation and numerical colour reallocation.

The collision step acts on the mixed fluid's distribution function f_i,

$$f_i(\boldsymbol{r}, t) = \sum_{\alpha=0}^{N_Q-1} f_i^\alpha(\boldsymbol{r}, t), \tag{3.1}$$

exactly after Zou *et al.* (1995), except with an effective relaxation parameter defined to give a mixed-fluid mean viscosity

$$\nu(\boldsymbol{r}, t) = \frac{1}{\rho(\boldsymbol{r}, t)} \sum_{\alpha=0}^{N_Q-1} \rho^\alpha(\boldsymbol{r}, t) \nu^\alpha,$$

where ν_α defines the chosen kinematic viscosity of component α of the node at $\boldsymbol{r}$, which relates to a particular ν^Γ through the colour map $l(\boldsymbol{r}, i, \alpha)$, and

$$\rho(\boldsymbol{r}, t) = \sum_{\alpha=0}^{N_Q-1} \rho^\alpha(\boldsymbol{r}, t), \qquad \rho^\alpha(\boldsymbol{r}, t) \equiv \sum_{i=0}^{Q-1} f_i^\alpha(\boldsymbol{r}, t).$$

Preventing coalescence amounts to dealing consistently with all possible mixed-node colour states using generalized perturbing and recolouring processes that eliminate mixing between all pairs of species, which may be stated as a need to maximize the work done by a generalized colour flux against a generalized colour gradient. Accordingly, the diphasic Gunstensen colour gradient is generalized for the interface between fluid α and fluid β, by what we assume to be its local normal (Dupin *et al.* 2003):

$$\boldsymbol{I}_{\alpha\beta}(\boldsymbol{r}) = \sum_i (\rho^\alpha(\boldsymbol{r} + \boldsymbol{c}_i) - \rho^\beta(\boldsymbol{r} + \boldsymbol{c}_i)) \boldsymbol{c}_i. \tag{3.2}$$

This colour gradient is used to perturb the mixed fluids' distribution (equation (3.1)), with a surface tension inducing fluctuation. For the interface between two components α and β we use a generalized perturbation,

$$\Delta f_i^{\alpha\beta}(\boldsymbol{r}, t) = \sigma_{\alpha\beta} C_{\alpha\beta}(\boldsymbol{r}, t) \cos(2(\theta_f(\boldsymbol{r}) - \theta_i)), \tag{3.3}$$

in which there is no summation on repeated subscripts, $\sigma_{\alpha\beta}$ is a surface-tension parameter for the $\alpha\beta$ interface and

$$C_{\alpha\beta}(\boldsymbol{r}, t) = 1 - \left| \frac{\rho_\alpha(\boldsymbol{r}, t) - \rho_\beta(\boldsymbol{r}, t)}{\rho_\alpha(\boldsymbol{r}, t) + \rho_\beta(\boldsymbol{r}, t)} \right|, \tag{3.4}$$

is the generalized *concentration factor* for the α, β fluid pair which limits the action of surface tension to multi-coloured nodes (Thompson *et al.* 1999). For a D2Q9 lattice (see figure 2), $\sigma_{\alpha\beta}$ is modulated by the factor λ_0, so that $\sigma_{\alpha\beta}$ becomes

$$\sigma_{\alpha\beta}^i = \begin{cases} \lambda_0 \sigma_{\alpha\beta} & i \text{ even}, \\ \sigma_{\alpha\beta} & i \text{ odd}, \end{cases}$$

It has been found that $\lambda_0 \approx 2.12$ provides the best angular isotropy of the drop (Dupin *et al.* 2003). This maximization of the drop's isotropy ensures that radial interfacial tension is uniform, but has other beneficial effects: the micro-current flow is minimized. To confirm the value 2.12, the qualitative features of the micro-current flow field of an enclosed drop may be predicted: by considering the (angular) directions in which the perturbation (3.3) produces the minimum flow in the near-interfacial region, the factor $\lambda_0 = 3/\sqrt{2}$ is given (as shown in Dupin *et al.* (2003)).

We now define an 'average' colour gradient which points towards component α and away from the total of all other components present at the node at position $\boldsymbol{r}$:

$$\boldsymbol{f^\alpha}(\boldsymbol{r}) = \sum_i \sum_j \left[f_j^\alpha(\boldsymbol{r} + \boldsymbol{c}_i) - \sum_{\beta \neq \alpha} f_j^\beta(\boldsymbol{r} + \boldsymbol{c}_i) \right] \boldsymbol{c}_i$$

$$\boldsymbol{f^\alpha}(\boldsymbol{r}) = \sum_i [2\rho^\alpha(\boldsymbol{r} + \boldsymbol{c}_i) - \rho(\boldsymbol{r} + \boldsymbol{c}_i)]\boldsymbol{c}_i. \tag{3.5}$$

The same calculation is repeated for each pair of fluid components $\alpha\beta$ present at the node, position $\boldsymbol{r}$, the appropriate colour gradient $\boldsymbol{f}^\alpha(\boldsymbol{r})$ (equation (3.5)) being used to 're-colour' (see below) for component α within each node, essentially in the same way as for a binary fluid but with the order in which components α are treated begin significant (see below). Accordingly, the total perturbation applied to the mixed fluid at the node at position $\boldsymbol{r}$ is

$$\Delta f_i(\boldsymbol{r}, t) = \sum_{(\alpha, \beta)} \Delta f_i^{\alpha, \beta}(\boldsymbol{r}, t), \tag{3.6}$$

in which the summation is taken on all possible pairs α, β and $\Delta f_i^{\alpha, \beta}(\boldsymbol{r}, t)$ is defined in equation (3.3). Note that calculation of the colour gradient (3.5) requires knowledge of the absolute colour, not just the relative amounts of the different colours present in a local environment. The sum on α of these individual fields is a measure of the local gradient in the total fluid density and is therefore zero only in a uniform fluid.

The perturbation process produces surface-tension effects in the hydrodynamics but it does not segregate the mixed fluids. To achieve segregation, a process of 're-colouring' is used. The (conserved) masses of the individual colours present at any mixed fluid site are numerically re-allocated to the post-perturbed f_i, so as to return as much of species α as possible up the gradient $\boldsymbol{f}^\alpha$, defined in equation (3.5).

In order to achieve optimal colour separation, the order of the reallocation of more than two colours to receptacle f_i is significant. Different ordering in the re-colouring process can clearly result in small differences in the post-collision, post-segregated state. Careful observation shows that these differences are small but not without consequence. In order to produce optimum segregation (sharp interface), the minority species at a node is given *priority* allocation to its favoured direction. Failure to adopt this scheme results in a relatively large loss of information about the location of minority species, resulting in small but undesirable adhesion between drops in contact.

Target flow applications are, by intention, heavily interface dominated. For the effectively mono-disperse systems we shall consider here, a maximum of five drops and ambient fluid in immediate proximity was allowed (again, simple packing considerations mean this value will increase with increasing poly-dispersity). Resolving
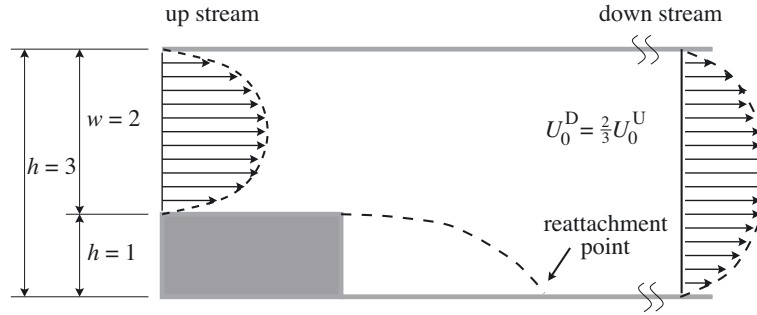
Figure 4. Geometry for a backward-facing step in channel flow with a step to channel width ratio of $\frac{1}{3}$. Both upstream and downstream of the step, flow behaves as standard Poiseuille flow. The step region introduces a recirculation zone of length L, the point of reattachment being when the x-component of the velocity changes sign. In two dimensions, the z-direction (into the plane of the paper) is infinite and so does not influence the flow.

five immiscible drops or de-mixing fluids leads to a maximum of $_2P_5 = 10$ *possible* local interfaces. Having selected a resolution, however, it is crucial to note that we have shown that execution-time and memory requirements scale only weakly with N, the number of components or drops (Dupin *et al*. 2003).

In high-volume-fraction flows, drops can come close to the simulation boundary and to each other. As an initial step, to avoid the need to postulate sub-lattice lubrication forces, we encourage an explicit layer of ambient liquid always to remain between drops and the boundary. We therefore need to ensure preferential wetting of the boundary and suspended drops by the ambient fluid. This was achieved for the simulations described here (Dupin *et al*. 2004). But the role of lubrication forces is quite possibly important in high-volume-fraction suspensions of deformable particles, for intimate contact is inevitable. As we shall discuss below, the applications considered in the results of figures 8–15 are designed to assist in determining this validity of this assumption.

4. Results: single and N-component pressure-driven flows

We first investigate laminar pressure-driven flow properties of a single-component fluid over a backward-facing step using two different LBM methods. Steady-state results from EILBGK simulation and from body-forced LBGK are compared with experimental data (Denham & Patrick 1974). We proceed to simulate N-component pressure-driven flow in similar internal geometries, concentrating on issues which relate to the transport of deformable particles, such as lift in a uniform shear and shear banding of a suspension.

(a) Laminar flow over a backward-facing step

The backward-facing step geometry (figure 4) produces flow separation at the step and subsequent re-attachment, which is recognized as important within industrial situations.

We consider a ratio of step height to downstream channel width of $\frac{1}{3}$, for which there exist two independent experimental investigations approximating two-dimensional flow (Denham & Patrick 1974; Kueny & Binder 1984). Other LBM

simulations originate with Qian *et al.* (1996), who investigate the relationship of the length of the recirculation zone and *Re*. Chen *et al.* (1997) give a thorough quantitative comparison of simulation results with experimental data from Kueny & Binder (1984). Here we concentrate on a quantitative comparison with data from Denham & Patrick (1974).

Results were obtained for a range of Reynolds numbers using two methods, both assuming two-dimensional flow. Our first method uses standard LBGK in D2Q9 with second-order accurate mid-link bounce-back 'solid' boundaries (figure 4), periodic boundaries in the direction along the pipe and forcing with a conservative body-force to approximate the principal part of the pressure field. No pressure gradient is set explicitly. The overall pressure field is extracted as described below. Using this method the 'pressure term' $(-c_s^2 \partial_\alpha \rho)$, in the lattice Navier–Stokes equation (2.2), is regarded as a correction to a principal pressure field which is the potential function for the appropriate body force. The body force in the narrow part of the channel is $\frac{27}{8}$ times that of the wide part of the channel, based upon matching parabolic flow rates. The potential function for this conservative body-force field is

$$\Phi(x) \equiv \begin{cases} -\frac{27}{8} Gx, & x < x_0, \\ -G(x + \frac{27}{8} x_0), & L > x > x_0, \end{cases} \tag{4.1}$$

in which G is the adjustable force constant and x_0 the step length. The pressure field of the body-forced LBGK (below) is now determined by the expression $c_s^2 \rho + \Phi$. Mass is strictly conserved, and pressure across the width of the inlet and outlet throats was held constant. The length of the lattice was chosen to minimize compressibility errors (which may be measured from the velocity divergence in the steady-state continuity equation

$$\partial_\alpha u_\alpha = -\frac{u_\alpha}{\rho} \partial_\alpha \rho$$

but are otherwise ignored here).

Our second method uses the exactly incompressible EILBGK model, which allows pressure and velocity boundary conditions to be applied more accurately at the inlet and outlet throats. Again non-slip boundaries are invoked using mid-link bounce back. Flow is now induced by setting discharge-matched parabolic velocity profiles at inlet and outlet and by fixing the outlet pressure while allowing the inlet pressure to develop to accord with the necessary pressure gradient (itself an observable). Because of direct link between lattice density and pressure, the total mass of this simulation increases asymptotically to a steady-state value.

Using the law of similarity, we compare body-forced LBGK and EILBGK simulations with experimental results from Denham & Patrick (1974), based on Denham's definition of *Re*:

$$Re = \frac{\bar{U} h}{\nu}, \tag{4.2}$$

in which $\bar{U}$ is the average flow velocity upstream of the step, h step height and ν the kinematic viscosity. Comparison of simulated and experimental data was made by normalizing velocities to the appropriate $\bar{U}$, distances to the step height h. For all our velocity data we note that both the body-forced LBGK and EILBGK results give very similar results for given *Re*, so velocity figures are representative of both models
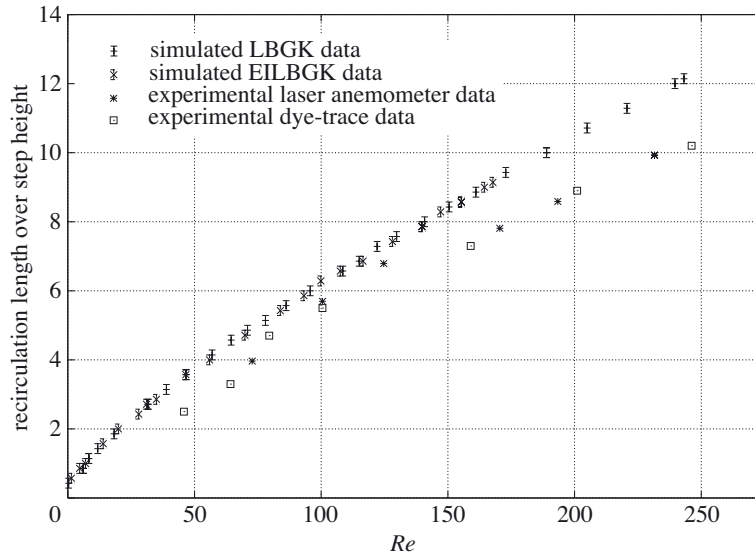
Figure 5. The recirculation length as a function of Re for the expansion ratio $\frac{1}{3}$. Data are compared with experimental values obtained via dye trace and laser anemometer measurements in Denham & Patrick (1974).

used. For all velocity data, flow profiles in the inlet and outlet were in good agreement compared with parabolic flow, supporting the assumption of fully developed flow. All results are analysed in their steady-state solutions, found by measuring the residual

$$R(t) = \sum_{\boldsymbol{x}} |\boldsymbol{u}(\boldsymbol{x}, t)|. \tag{4.3}$$

For the EILBGK system there is an additional condition on the total mass, which must be constant at steady state.

From stream-function data, the recirculation zone was seen to increase with increasing Re. The position of the vortex centre is given by the coordinates ($x_c = 0.3L_R, y_c = 0.6h$); this is in agreement with the coordinates given by Denham & Patrick (1974).

We define the recirculation length to be the distance x from the step at $y = 0$ in which a change in the x-velocity direction occurs. Figure 5 displays normalized recirculation length against Re for the step ratio of $\frac{1}{3}$. Note that the LBGK data provided in figure 5 are more accurate and cover a greater range of Re than in previous studies (Qian *et al.* 1996).

Both LBGK and EILBGK data are in good agreement. For given lattice resolution it was observed that the range of accessible Re for EILBGK is less than those for body-forced LBGK, owing to a more stringent incompressibility constraint. The experimental data points, taken from Denham & Patrick (1974), contain a $\pm 2\%$ tolerance for measurements of velocity. Including the tolerance limits, experimental results lie just below the simulated points, the discrepancy increasing as Re increases. But CFD simulations agree with our LBM models.

Velocity profiles obtained at different locations along the simulation are compared with experimental velocity profiles in figure 6. Recall that the agreement between
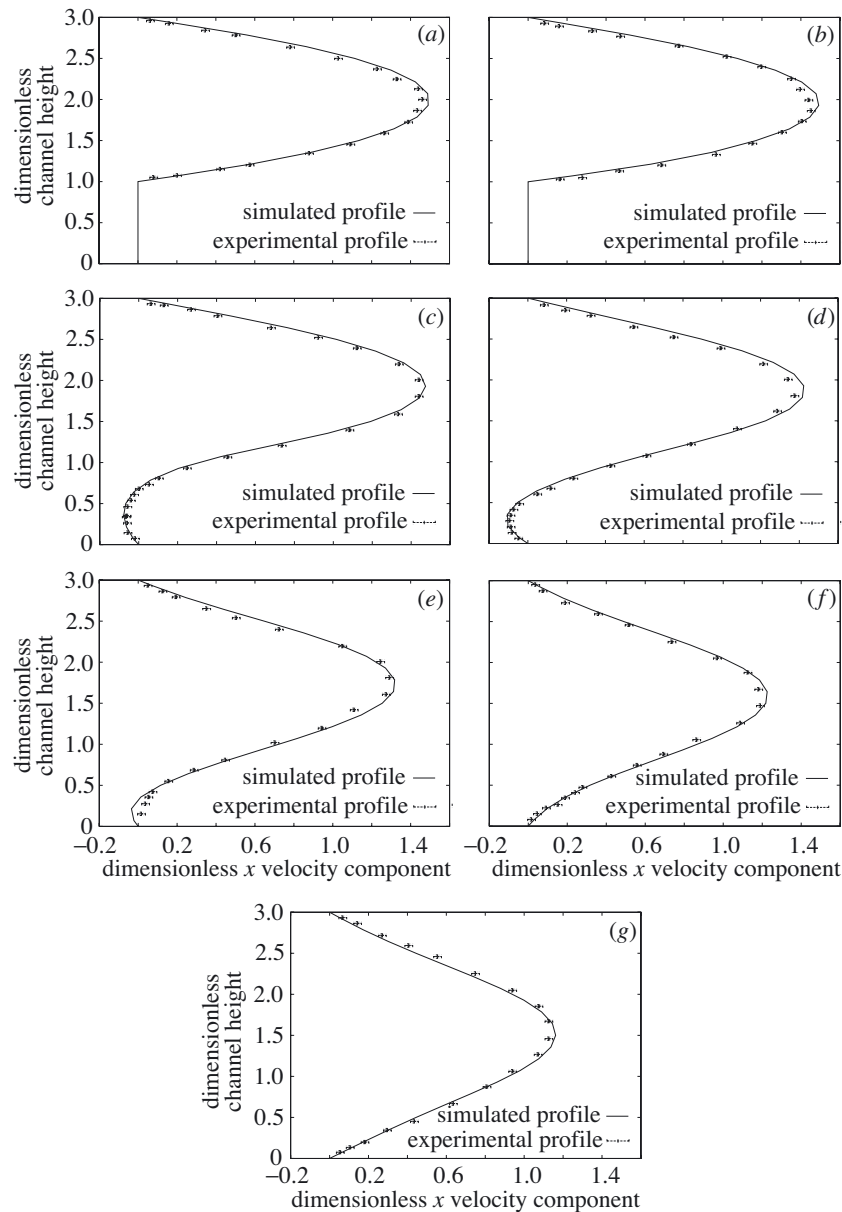
Figure 6. Comparison of simulated velocity profiles with experimental profiles obtained in Denham & Patrick (1974) in the step region at $Re = 73$ for various dimensionless distances from the step position: (*a*) -1.3, (*b*) 0.0, (*c*) 0.8, (*d*) 2.0, (*e*) 4.0, (*f*) 6.0 and (*g*) 8.0.

EILBGK and body-forced LBGK data is good and figure 6 shows only one set of simulation data, which agrees satisfactorily with experimental results at $Re = 73$. Upstream of the step, discrepancies are probably due to an inadequate development length in the experimental inlet (Denham & Patrick 1974). At higher Re, there emerge further discrepancies throughout the length of the system, probably due to
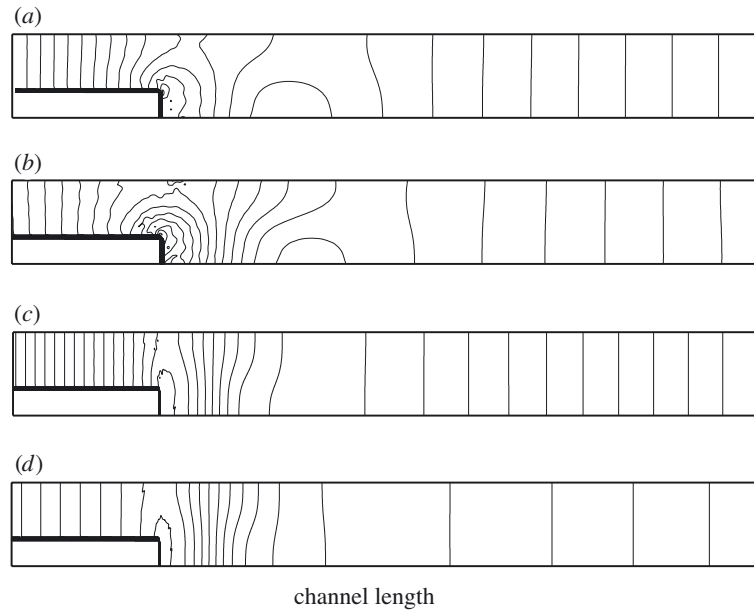
Figure 7. Pressure contours for (*a*), (*b*) $Re = 31$ and (*c*), (*d*) $Re = 174$ for (*b*), (*d*) body-forced LBGK and (*a*), (*b*) pressure-driven EILBGK. Both simulations used identical velocity boundary conditions (refer to text) but only in the EILBGK simulation does inlet pressure develop freely. There is qualitative agreement between the pressure fields (e.g. minimum pressure occurring in the recirculation zone for both simulations).

three-dimensional effects (Denham & Patrick 1974). More recent experiments on a backward-facing step with a step ratio of $\frac{1}{2}$ (Armely *et al*. 1983) support this conclusion.

Figure 7 shows steady-state pressure contours (with constant increment, in arbitrary units) for different Re, for body-forced LBGK and pressure-driven EILBGK. The step height is one-third of the width of the channel. The lattice size is 60×600. Recall that it is EILBGK which accommodates pressure boundary conditions, with inlet pressure developing freely. Qualitative agreement is good, with the minimum pressure occurring in the recirculation zone for both simulations. Notwithstanding this, there are small quantitative differences between these pressure fields of the same order as those which routinely appear between CFD solutions obtained by different methods. Unfortunately, no experimental information on the pressure exists.

As can be seen from figure 7, our two methods produce slightly different pressure contours. However, given their very different representations of a pressure field, the correspondence between the results is highly reassuring. Body-forced LBGK implementation essentially assumes a uniform gradient of pressure which is perturbed. While intuitively valid at most points in the simulation domain, this assumption is weak in the step region, where forced LBGK and EILBGK show differences.

(*b*) *Suspensions of deformable particles*

We proceed to consider pressure-driven flow of deformable particles, modelled as incompressible liquid drops, of varying volume fraction. The solid properties of our
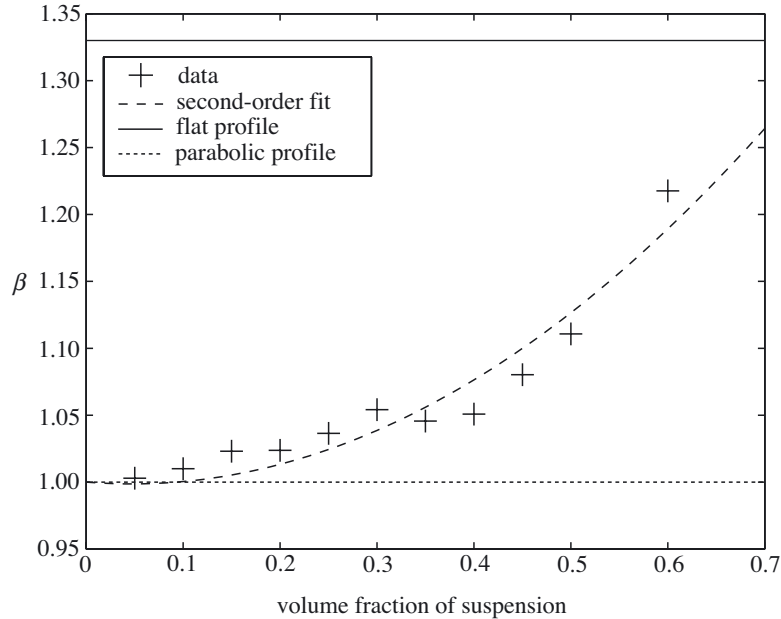
Figure 8. The increased blunting of a dense, monodisperse suspension's velocity profile with increased volume fraction ϕ, with fixed drop deformability. The latter is quantified by surface tension (parameter $\sigma = 0.01$) and viscosity ratio $\Lambda = 30$ and fixed flow rate (pressure gradient). ϕ varies over the range 0.1–0.6. The latter value is determined by packing and lubrication considerations.

particles are controlled through their interfacial tension and viscosity relative to that of the ambient fluid, Λ. The latter is parametrized by $\Lambda \leqslant 50$ and controlled as discussed in the last section. Figures 8–12 demonstrate our N-phase algorithm applied to pressure-driven duct flow of a dense suspension of neutrally buoyant drops. On inspection, our blunted profiles have noticeable departure from parabolic. We assess averaged departure, at normalized cross-duct distances $\bar{y} = 0.25$ and $\bar{y} = 0.75$ by defining a blunting β:

$$\beta \equiv \frac{\bar{v}(\bar{y} = 0.25) + \bar{v}(\bar{y} = 0.75)}{2 \times 0.75}, \tag{4.4}$$

in which 0.75 is the height of a normalized parabola. With this definition, a flat velocity profile is characterized by $\beta = 1.33$ and a parabolic velocity profile by $\beta = 1.00$.

A lattice of size 100×250 containing drops of initial radii 4 lattice units was used. Data were extracted from steady-state configuration (typically 1.0×10^5 simulation time-steps). The upper and lower dot-dashed lines in figures 8 and 9 illustrate the value of β corresponding to a flat and a parabolic velocity profile, respectively. The dashed line represents a second-order interpolation to the data. Details of each simulation are to be found in the appropriate caption.

For rigid suspended particles it is known that the velocity profile is determined solely by the suspension concentration and the relative particle size (Caro *et al*. 1998). By setting $\Lambda = 50$ (large) and increasing the volume fraction of suspended material we can obtain the expected increase in β (figure 8). We note that no significant
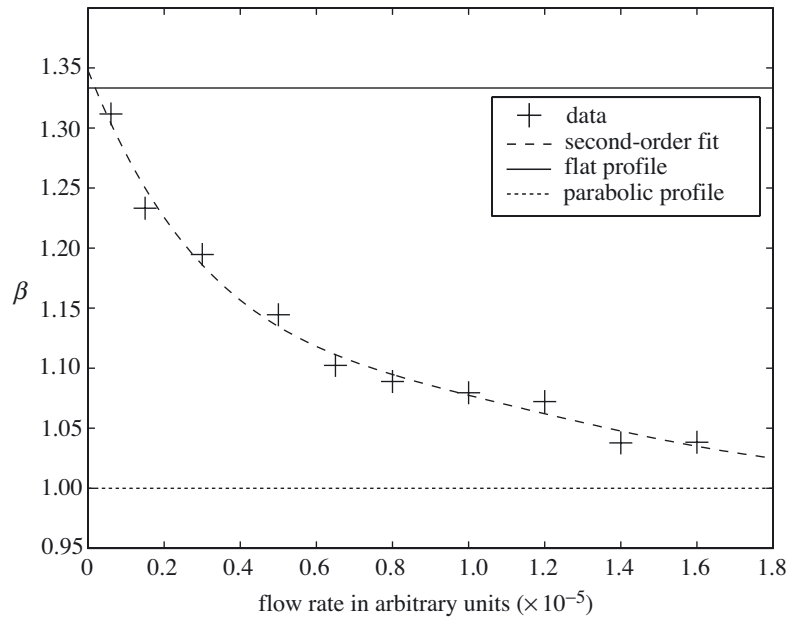
Figure 9. The decrease of blunting with increasing pressure gradient ΔP with non-constant deformability. Fixed surface tension (parameter $\sigma = 0.005$) and viscosity ratio $\Lambda = 1$.

changes in β were observed for constant volume fraction, on increasing pressure difference, as expected.

For immiscible liquid drops (i.e. flexible particle suspensions, $\Lambda = 1$), on the other hand, we observe the expected dependence of the velocity profile upon the flow rate (applied pressure gradient), with the degree of blunting decreasing as flow rate increases (Caro *et al.* 1998) (figure 9).

In both figures 8 and 9 the expected qualitative features tend to vindicate the method we have used to circumvent lubrication forces (see the last section). The qualitatively correct nature of the variation in the macroscopic suspension flow profiles emerges from the microscopic rules implemented. In particular our device of enforcing an explicit layer of ambient fluid at drop and boundary surfaces seems to be valid, at volume fraction $\phi = 0.6$ at least.

Recent experimental data confirm the shear-induced positional ordering of dense, intimate suspensions of particles and drops (Frank *et al.* 2003). Figure 10 shows the time-development of the cross-duct location of all the drop centres in an initially randomly placed suspension.

Clearly, starting from a random configuration (figure 11), and after an initial phase of transverse migration, our dense mono-disperse suspension of drops tends to flow in well-defined horizontal layers (figure 12), with occasional 'hopping', giving rise to an effective transverse diffusion of suspended drops.

(c) Lift of deformable particles with linear shear

Liquid drops deform and certainly do not transmit stresses instantaneously. To compare the properties of liquid and solid drops as components in a microscopic model of transport we consider particle lift. Particles of radius R confined in channels
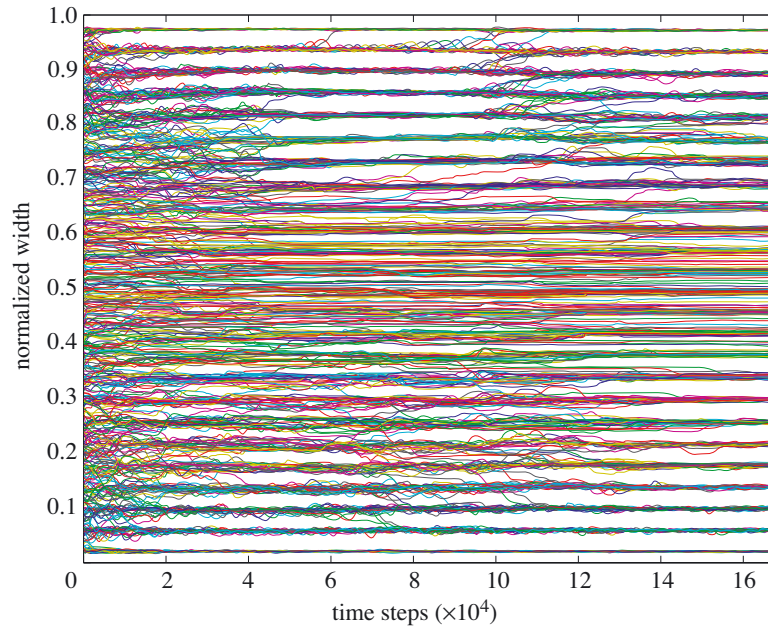
Figure 10. Trajectories of drop centres in time. Drop surface-tension parameter $\sigma = 0.005$ and viscosity ratio $\lambda = 1$. The suspended drop volume fraction was 0.6: the lattice size was 250×100 and the drop radius was 4.
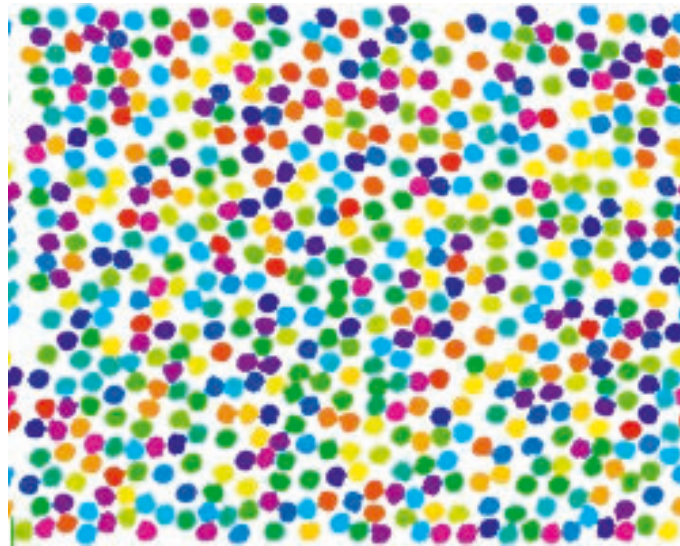

Figure 11. Random initial arrangement of the droplets.

and subject to flow (here a linear shear $\dot{\gamma}$) tend to migrate away from the wall, eventually to advect at some distance from the wall characteristic of the particle Reynolds number:

$$Re_{\mathrm{p}} = \frac{\dot{\gamma} R^2}{\nu}. \tag{4.5}$$

Figure 12. Steady state of the suspension of rigid droplets showing banding and ordering.
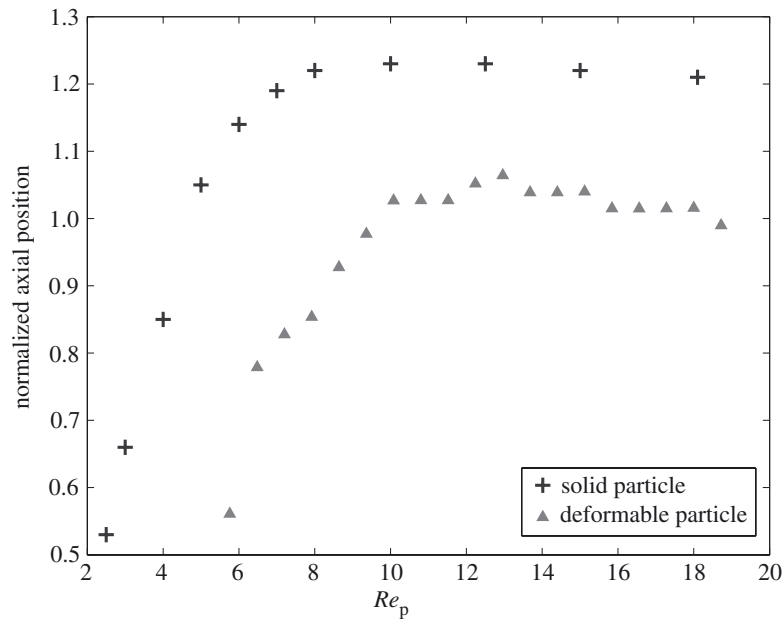

Figure 13. Steady-state elevation of a single droplet in straight channel
normalized to its diameter with the particle Reynolds number.

Figure 13 shows the lift (normalized cross-duct displacement) of a neutrally buoyant deformable drop, $\Lambda = 10$, for reference, and a solid cylindrical particle of the same size, for a range of Re_{p}.

The latter was simulated by the LBM using the algorithm of Ladd (1994). Simulation parametrization for both solid and deformable drops is as specified in the figure caption. The geometry of both simulations was identical. As expected, there

is a some difference between the two objects—a relatively low viscosity drop has an internal flow structure and a different drag. However, within the bounds of simulation error, both solid and deformable drop data show qualitative similarities in the overall shape of the graphs. Note also that the range of accessible Re_p is appreciable.

5. Conclusion

In § 2 of this paper we have derived governing hydrodynamical equations for single-component LBMs and in § 3 we detailed the most recent N-component extension, predicated on continuum length-scale applications to large numbers of explicitly modelled deformable bodies.

The lattice Boltzmann technique appears to present a numerical scheme for the simulation of complex, N-component hydrodynamics. In particular it holds out the prospect of realistic simulations, at the continuum length-scale, of high-volume-fraction suspensions of deformable drops, currently modelled as drops of relatively viscous, incompressible fluids.

We present results for pressure-driven flow in internal geometry, demonstrating and validating an efficient single-component implementation (the backward-facing step) and an N-component extension (chaining, lift). For many engineering computations in the lattice Boltzmann literature, flow is induced by a uniform body forced method for easier algorithmic implementation. Our single-component results suggest that, if only velocity information is required, then this method may be used with confidence and, with appropriate adjustment, can produce a good representation of the pressure field. Our multi-component results, we suggest, point to N-component lattice Boltzmann simulation as a very useful tool for the explicit modelling of transport in dense suspensions.

For the future, our model should be improved by the inclusion of lubrication forces, which assume increasing importance as the suspended material volume fraction increases. At low volume fraction, suspended particles will, broadly, advect with the flow, embedded in the local fluid. Accordingly, the properties of the interface with low tangential and normal stresses, especially in respect of the micro-current activity assume greater significance. For micro-fluidic applications, to which all the methods reported here apply, this micro-current is, again, of considerable importance. It is our opinion that the most significant challenge to application of the N-component lattice Boltzmann computation is accurate representation of the interface.

References

Abe, T. 1966 *J. Comput. Phys.* **131**, 241–246.

Alexander, F. J., Chen, S. & Sterling, J. D. 1993 *Phys. Rev.* E **47**, 2249–2252.

Allen, M. P. & Tildesley, D. J. 1997 *Computer simulation of liquids.* Oxford: Clarendon.

Anderson, J. D. 1995 *Computation fluid dynamics: the basics with applications.* McGraw-Hill.

Armely, B. F., Durst, F., Pereira, J. C. F. & Schönung, B. 1983 *J. Fluid Mech.* **127**, 473–496.

Benzi, R., Succi, S. & Vergassola, M. 1992 *Phys. Rep.* **222**, 145–197.

Bhatnagar, P. E., Gross, P. E. & Krook, M. 1954 *Phys. Rev.* A **94**, 511–525.

Boghosian, B. & Taylor, W. 1997 *Int. J. Mod. Phys.* C **8**, 705–716.

Broadwell, J. E. 1964 *Phys. Fluids* **7**, 1243–1247.

Cali, A., Luo, L. S., Cancelliere, A., Benzi, R. & Gramignani, M. 1992 *Phys. Rev.* A **45**, 5771–5774.

Caro, C. G., Pedeley, T. J., Schroter, R. C. & Seed, W. A. 1998 *The mechanics of the circulation.* Oxford Medical Publications.

Chapman, S. & Cowling, T. G. 1970 *The mathematical theory of non-uniform gases*, 3rd edn. Cambridge University Press.

Chen, H., Chen, S. & Matthaeus, W. H. 1992 *Phys. Rev.* A **45**(8), 5339–5342.

Chen, S. & Doolen, G. D. 1998 *A. Rev. Fluid Mech.* **30**, 329–364.

Chen, S., Chen, H., Martinez, C. & Matthaeus, W. 1991 *Phys. Rev. Lett.* **67**(27), 3776–3779.

Chen, Y., Ohashi, H. & Akiyama, M. 1997 *JSME Int. J.* B **40**(1), 25–32.

Chen, Y., Ohashi, H. & Akiyama, M. 1994 *Phys. Rev.* E **50**(4), 2776–2783.

Conner, J. & Brebbia, C. 1976 *Finite element techniques for fluid flow.* Woburn, MA: Newnes– Butterworth.

Denham, M. K. & Patrick, M. A. 1974 *Trans. IChE* **52**, 361–367.

D'Humières, D., Lallemand, P. & Qian, Y. H. 1989 *Review of flow simulations using lattice gases.* Lecture Notes in Mathematics, vol. 1402, pp. 56–58. Springer.

Do-Quang, M., Aurell, E. & Vergassola, M. 2000 An inventory of lattice Boltzmann models of multiphase flows. Technical Report, ISSN 0348-467X. (Available at http://www.psci.kth.se/ Activities/Reports/Results/R_2000_03/psci2000_03.pdf.)

Dupin, M. M., Halliday, I. & Care, C. M. 2003 Multi-component lattice Boltzmann equation for mesoscale blood flow *J. Phys.* A **36**, 8517–8534.

Dupin, M. M., Halliday, I. & Care, C. M. 2004 A lattice Boltzmann model of flow blunting. *Phil. Trans. R. Soc. Lond.* A **362**, 1755–1761.

Español, P. 2002 *SIMU Newsletter*, issue 4, ch. III, pp. 59–77. (Available at http://simu. ulb.ac.be/newsletters/N4III.pdf.)

Ferreol, B. & Rothman, D. H. 1995 *Transport Porous Media* **20**, 3–20.

Filippova, O. & Hanel, D. 1998 Grid refinement for lattice-BGK models. *J. Comput. Phys.* **147**, 219–228.

Frank, M., Anderson, D., Weeks, E. R. & Morris, J. F. 2003 *J. Fluid Mech.* **493**, 363–378.

Frisch, U., Hasslacher, B. & Pomeau, Y. 1986 *Phys. Rev. Lett.* **56**, 1505–1508.

Goodfellow, J. 1991 *Molecular dynamics.* London: Macmillan.

Groot, R. D. & Warren, P. B. 1997 *J. Chem. Phys.* **107**, 4423–4435.

Gunstensen, A. K., Rothmann, D. H., Zaleski, S. & Zanetti, G. 1991 Lattice Boltzmann model of immiscible fluids. *Phys. Rev.* A **43**(8), 4320–4327.

Halliday, I., Care, C. M. & Thompson, S. P. 1998 Macroscopic surface tension in a lattice Bhatnagar–Gross–Krook model of two immiscible fluids. *Phys. Rev.* E **57**, 514–523.

Halliday, I., Hammond, L. A., Care, C. M., Good, K. & Stevens, A. 2001 Lattice Boltzmann equation hydrodynamics. *Phys. Rev.* E **64**, 011208.

Halliday, I., Hammond, L. A. & Care, C. M. 2002 *J. Phys.* A **35**, 157–166.

Hardy, J., Pomeau, Y. & De Pazzis, O. 1973 *J. Math. Phys.* **14**, 1746–1759.

Hardy, J., De Pazzis, O. & Pomeau, Y. 1976 *Phys. Rev.* A **13**, 1949–1961.

He, X. & Doolen, G. D. 1997*a Phys. Rev.* E **56**, 434–440.

He, X. & Doolen, G. D. 1997*b J. Comput. Phys.* **134**(2), 306–315.

He, X. & Luo, L. S. 1997*a Phys. Rev.* E **55**(6), 6333–6336.

He, X. & Luo, L. S. 1997*b Phys. Rev.* E **56**(6), 6811–6817.

He, X., Zou, Q., Luo, L. S. & Dembo, M. 1997*a J. Stat. Phys.* **87**, 115–136.

He, X., Luo, L. S. & Dembo, M. 1997*b Physica* A **239**, 276–285.

Higuera, F. & Luo, L. S. 1989 *Europhys. Lett.* **8**, 517–521.

Hoogerbrugge, P. J. & Koelman, J. M. V. A. 1992 *Europhys. Lett.* **19**, 155–160.

Hou, S. 1995 PhD thesis, Kansas State University, Manhatten, KS, USA.

Hou, S., Zou, Q., Chen, S. & Doolen, G. D. A. C. 1995 *J. Comput. Phys.* **118**, 329–347.

Hou, S., Sterling, S. & Doolen, G. D. 1996 *Fields Inst. Commun.* **6**, 151–166.

Kadanoff, L. P., McNamara, G. R. & Zanetti, G. 1989 *Phys. Rev.* A **40**(8), 4527–4541.

Kueny, L. J. & Binder, G. 1984 Viscous flow over backward facing steps: an experimental investigation, analysis of laminar flow over a backward facing step. *Not. Fluid Mech.* **9**, 32–42.

Ladd, A. J. C. 1994 *J. Fluid Mech.* **271**, 311–339.

Landau, L. D. & Lifshitz, E. M. 1995 *Fluid mechanics*. Course in Theoretical Physics, 2nd edn, vol. 6. Oxford: Butterworth-Heinemann.

Liboff, R. C., Herman, J. & Liboff, R. L. 2003 *Kineic theory*, 2nd edn. Springer.

Lin, Z., Fang, H. & Tao, R. 1996 *Phys. Rev.* E **54**(6), 6323–6330.

Lishchuk, S. V., Care, C. M. & Halliday, I. 2003 *Phys. Rev.* E **67**, 036701.

Luo, L. S. 1998 *Phys. Rev. Lett.* **81**(8), 1618–1621.

Luo, L. S., Wang, J. & Qian, Y. H. 1997 *Int. J. Mod. Phys.* C **8**(4), 999–1008.

Luo, L. S. 2000 *Phys. Rev.* E **64**(4), 4982–4996.

McNamara, G. R. & Zanetti, G. 1988 *Phys. Rev. Lett.* **61**(20), 2332–2335.

Maier, R. S., Bernard, R. S. & Grunau, D. W. 1996 *Phys. Fluids* **8**(7), 1788–1801.

Martinez, D. O., Chen, S. & Matthaeus, W. H. 1994 *Phys. Plasmas* **1**, 1850–1867.

Mei, R., Shyy, S., Yu, D. & Luo, L. S. 2000 *J. Comput. Phys.* **161**, 680–699.

Noble, D. R., Georgiadis, J. G. & Buckius, R. O. 1995 *J. Stat. Phys.* **81**, 17–33.

Qian, Y. H. & Zhou, Y. 1998 *Europhys. Lett.* **42**(4), 359–364.

Qian, Y. H., D'Humières, D. & Lallemand, P. 1992 *Europhys. Lett.* **17**(6), 479–484.

Qian, Y. H., Luo, L. S., Massaioli, F. & Orszag, S. A. 1996 *Fields Inst. Commun.* **6**, 207–215.

Reider, M. B. & Sterling, J. D. 1995 *Comput. Fluids* **24**, 459–467.

Rothmann, D. H. & Zaleski, S. 1994 *Rev. Mod. Phys.* **66**(4), 1417–1479.

Shan, X. W. & Chen, H. D. 1994 *Phys. Rev.* E **49**(4), 2941–2948.

Skordos, P. A. 1993 *Phys. Rev.* E **48**(6), 4823–4842.

Spencer, T. J., Dupin, M. M., Halliday, I. & Care, C. M. 2004 An incompressible Lattice BGK scheme with enhanced stability. (In preparation.)

Succi, S. 2001 *The lattice Boltzmann equation*. Oxford: Clarendon.

Succi, S. 2002 *Phil. Trans. R. Soc. Lond.* A **360**, 429–436.

Succi, S., Foti, E. & Higuera, F. 1989 *Europhys. Lett.* **10**, 433–438.

Succi, S., Benzi, R. & Higuera, F. 1991 *Physica* D **47**, 219–230.

Swift, M. R., Osborn, W. R. & Yoemans, J. M. 1995 *Phys. Rev. Lett.* **75**(5), 830–833.

Thompson, S. P., Halliday, I. & Care, C. M. 1999 Mesoscopic hydrodynamics of diphasic lattice Bhatnagar–Gross–Krook fluid interfaces. *Phys. Chem. Chem. Phys.* **1**, 2183–2190.

Tölke, J., Krafczyk, M., Schultz, M., Rank, E. & Berrios, R. 1998 *Int. J. Mod. Phys.* C **9**, 1143–1157.

von Neumann, J. 1966 *Theory of self-reproducing automata*. University of Illinois Press.

Wagner, L. 1994 *Phys. Fluids* **6**, 3516–3518.

Wolfram, S. 1986 *Rev. Mod. Phys.* **55**, 601–644.

Yang, Z. L., Dinh, T. N., Nourgaliev, R. R. & Sehgal, B. R. 2001 *Int. J. Heat Mass Transfer* **44**, 195–206.

Zou, Q., Hou, S., Chen, S. & Doolen, G. D. 1995 Analytical solutions of the lattice Boltzmann BGK model. *J. Stat. Phys.* **81**, 319–334.